Semiconductors, 2024, Vol. 58, No. 3

Thermoelectric properties of $CaMnO_3$ perovskite produced by spray solution combustion synthesis*

© E.V. Chernyshova, S.I. Roslyakov, Zh.S. Yermekova, E.V. Argunov, D.O. Moskovskikh, S.N. Yudin, V.V. Khovaylo

University of Science and Technology „MISIS“,
119049 Moscow, Russia

E-mail: evgeniachernyshova8@gmail.com

Received March 22, 2024
Revised April 15, 2024
Accepted April 15, 2024

$CaMnO_3$ powder was synthesized by spray solution combustion synthesis using glycine. Due to the highly exothermic reaction between the precursor components, spray solution combustion synthesis eliminates the calcination step and allows one to obtain a crystalline product in a few seconds. Consolidation was carried out using cold pressing followed by annealing in air. Single-phase $CaMnO_3$ showed a decrease in thermal conductivity relative to literature data, with the dominant mechanism of phonon scattering at grain boundaries. The mechanism of electrical conductivity is based on thermally activated small polarons hopping between localized states of Mn^{3+} and Mn^{4+}. Synthesized $CaMnO_3$ has high absolute values of the Seebeck coefficient, which leads to competitive efficiency values among both undoped and doped compositions but eliminates the use of expensive precursors.

Keywords: spray solution combustion synthesis, thermoelectric oxides, Calcium manganite, perovskites.

DOI: 10.61011/SC.2024.03.58836.33T

1. Introduction

The waste heat recovery for power generation is implemented using thermoelectric generators (TEG) operating in different temperature ranges. It is necessary to increase the thermoelectric efficiency of the materials from which these devices are made for increasing their efficiency. The parameter its figure of merit (zT) which is expressed by the formula (1):

$$zT = \frac{\alpha^2\sigma}{\kappa}T, \tag{1}$$

where α — Seebeck coefficient, σ — specific electrical conductivity, κ — thermal conductivity, T — absolute temperature.

Relatively high values of zT were achieved in compounds based on tellurium, antimony and germanium [1–3]. However, it is known that the stability and toxicity of these compounds are a limiting factor for some applications.

Oxide thermoelectrics do not have a high zT in comparison with traditional thermoelectric materials [4–6]. However, the results with competitive competitive zT values are known, for example, it was shown in Ref. [7] that the composite $SrTiO_3$ with natural graphite doped with niobium reaches $zT \sim 1.42$ at 1050 K. Moreover, oxide TE materials have advantages such as low cost of raw materials, environmental friendliness of production and chemical stability at high temperatures. Therefore, the issue of finding ways for increasing the efficiency of oxide thermoelectrics seems to be quite relevant.

$CaMnO_3$ (CMO) is considered as one of the promising oxides with *n*-type conductivity. The authors of Ref. [8] report a high value of $zT = 0.2$ achieved on niobium-doped CMO at 1020 K. However, the undoped $CaMnO_3$ is characterized by low TE characteristics [9–13], which is explained by the low mobility of charge carriers due to ionic bonding, which leads to strong scattering of electrons by optical phonons. On the contrary, the substitution of metal cations in the CMO lattice with various elements is one of the methods for regulating the structure of the material and can greatly reduce the resistivity, which improves the Thermoelectric characteristics [14]. Ytterbium is the most effective alloying element in the position of calcium. Its introduction into the CMO structure results in a significant increase of the electrical conductivity and Seebeck coefficient, at the same time a decrease of total thermal conductivity is observed, which is mainly attributable to the large mass difference between Yb^{3+} and Ca^{2+} [15]. A significant increase of electrical conductivity is also achieved by replacing manganese cations with niobium. However, a sharp decrease of Seebeck coefficient takes place along with an increase of electrical conductivity [16]. Complex alloying with different elements in one of the positions also turns out to be effective. For example, it was shown in Ref. [17] that the combination of heterovalent and homovalent substitution with a small amount of a doping element ensures an optimum thermoelectric properties of ceramics, and $zT = 0.15$ was achieved for $Ca_{0.94}Y_{0.04}Mg_{0.02}MnO_{3-\delta}$ at 973 K. There are also known studies with metal substitution at different positions simultaneously (for example, $Ca_{0.95}Yb_{0.05}Mn_{0.98}Nb_{0.02}O_3$), which allowed obtaining $zT = 0.13$ at 973 K [15]. Although doping is a generally recognized effective way to increase the efficient of TEG, however, the use of expensive precursors is a significant disadvantage of this approach.

---

* XVIII Interstate Conference THERMOELECTRICS AND THEIR APPLICATIONS — 2023 (ISCTA 2023)

Another approach aimed at increasing zT involves reducing thermal conductivity by modifying the micro- and nanostructure of oxide TE materials. This is achieved by varying the methods used for producing both powder materials and compact products. The transport characteristics of nanostructured bulk materials differ significantly from the properties of analogues with a coarse-grained structure. For example, it was shown that the thermal conductivity of oxide ceramics can be reduced by introducing nanoscale inclusions [18]. At the same time, the most common method for the synthesis of polycrystalline oxide TE materials based on a solid-phase reaction does not allow achieving such results, since the impurity phase particles are formed due to the relatively slow reaction rate, which subsequently increase thermal conductivity because of an increase of the free path of phonons.

On the contrary, the particle growth time is greatly reduced in powders prepared by the methods of „soft chemistry" (for example, various variations of the method of precipitation from solutions, sol-gel processes, processes in hydro- and solvothermal conditions, etc.) because of mixing of components at the molecular level and high nucleation rates.

There is a major disadvantage despite the advantages of „soft chemistry" methods over solid-phase synthesis — the complexity of scaling due to additional steps such as drying, filtration, leaching, calcination and grinding. The synthesis of materials by combustion of reaction aerosols (HA) [19], which combines the concepts of solution combustion synthesis and spray pyrolysis has significant advantages in comparison with the above approaches. The method makes it possible to obtain a crystalline product within a short period of time (seconds) and eliminate a long calcination stage due to the highly exothermic reaction between the precursor components.

Obtaining a given microstructure and stoichiometry by a specific method of synthesis of $CaMnO_3$ makes it possible to increase figure of merit not only by reducing thermal conductivity, but in this case also by optimizing electronic properties, electrical conductivity occurs due to electron hopping between Mn^{3+} and Mn^{4+} [20–22]. The ions of Mn^{3+} are generated due to the presence of oxygen vacancies [23].

In this study, spherical single-phase powders of CaMnO. thermoelectric material were obtained using a one-step combustion method of reactive aerosols, consisting of a homogeneous aqueous solution of an oxidizer (manganese and calcium nitrates with a Ca to Mn ion ratio of 1 : 0.95) and a reducer/fuel (glycine).

2. Materials and methods

The following precursors were used in this study: hydrated nitrates of metals Ca and Mn ($Ca(NO_3)_2 \cdot 4(H_2O)$, $Mn(NO_3)_2 \cdot 4H_2O$) used as oxidizing agents and sources of metal cations, and glycine ($C_2H_5NO_2$), used as an organic fuel/reducing agent. All precursors are high purity elements and were purchased from LLC TD „Khimmed". $CaMnO_3$ was obtained using the following scheme: One-molar (1 M) aqueous solutions of metal nitrates in a volume ratio of $Ca(NO_3)_2 \cdot 4H_2O : Mn(NO_3)_2 \cdot 4H_2O = 1 : 0.95$ were mixed in a ceramic beaker. Then a 1 M solution of fuel was added to the beaker and the resulting composition was thoroughly mixed for 30 minutes with a magnetic stirrer until a homogeneous solution was produced. The fuel to oxidizer ratio (φ), which means the molar ratio of fuel to the total number of moles of nitrates relative to stoichiometry, was 3. All calculations for preparing the solutions were based on the following chemical equation:

$$Ca(NO_3)_2 \cdot 4H_2O + Mn(NO_3)_2 \cdot 4H_2O + \varphi 2C_2H_5NO_2 = CaMnO_3 + 13H_2O + 6CO_2 + 3N_2. \quad (2)$$

A detailed technical information about the synthesis technique and a schematic representation of the experimental setup is provided in Ref. [24]. The prepared reaction solutions were placed in an inhaler chamber (IN 8, „Albedo"), where the aerosol was generated using a piezoelectric element with an operating frequency of 2.64 MHz. The aerosol droplets were sprayed into a tubular furnace with a stream of compressed air at a speed of 2 L/min. An exothermic combustion reaction occurred on the surface of a drop of the reaction solution as it flew through the hot zone of the furnace. A solid product was formed in the form of a black powder as a result of this reaction which was collected by a Schott filter located in the cold part of the set up. The temperature of the hot zone of the furnace was 1273 K. The $CaMnO_3$ powder was pressed for obtaining a compact sample by cold pressing at a pressure of 5 t into tablets with a diameter of 15 mm and a height of 4 mm, after which the obtained cylindrical samples were sintered for 4 hours in air at a temperature of 1473 K without applying pressure. The heating and cooling rates were controlled and maintained at 1 K/min.

The phase composition of the powders was studied by X-ray diffraction (XRD) room temperature using diffractometer DIFRAY-401 operating at a voltage of 25 kV and a current of 40 mA using a source of CrK_α-radiation with a Bragg-Brentano focusing geometry. Scanning electron microscope (SEM) JSM 7600F (JEOL, Japan) with a spatial resolution of $\sim$ 1 nm was use to study the morphology and general microstructure of products, provided with a system Oxford Instruments to study the elemental analysis (EDX) of products, as well for their elemental analysis.

Thermal diffusivity was measured using the laser flash method (thermal diffusivity analyzers LFA,447 NanoFlash (from 300 to 573 K) and NETZSCH LFA,457 MicroFlash (from 623 to 1023 K). Thermal conductivity (κ, W/(m · K)) was calculated using the formula

$$\kappa = \alpha \cdot C_p \cdot d, \quad (3)$$

where C_p — heat capacity, d — sample density. The density of the sintered sample was determined using the

Archimedes method using H_2O as an immersion liquid. The specific heat capacity was calculated using the Debye model. The Dulong-Petit law is fulfilled at high temperatures ($T \gg \theta_D$, where θ_D — Debye temperature, K):

$$C_p = 3 \cdot R \cdot M_r,$$

where R — universal gas constant, M_r — molar mass. The calculation of Debye temperature:

$$\theta_D = \frac{h\nu_m \left(3\,\frac{n}{4\pi MV}\right)^{1/3}}{k_B}, \tag{4}$$

where h — Planck's constant, ν_m — average speed of sound ($m \cdot s^{-1}$) [10], n — the number of atoms in the crystal cell, V — the volume of the unit cell ($Å^3$), was performed for the orthorhombic structure of the spatial group $Pnma$ (62). The value was $\theta_D = 650\,K$, which corresponds to the literature data [25].

The electrical resistivity and the Seebeck coefficient were measured simultaneously by four-probe and differential methods, respectively, on the equipment of LLC „CRYOTEL" in direct current mode.

3. Results and discussion

3.1. Characterization of the crystal structure and microstructure of the samples

The organic component added to the metal nitrate solution during the synthesis of materials by the method of combustion of reaction aerosols performs several important functions simultaneously: (i) a chelating component that binds metal cations in solution into a stable complex compound, which increases solubility and prevents selective precipitation of metal ions during synthesis; (ii) a fuel that provides sufficient heat to the system to ensure a self-sustaining reaction; (iii) a gasifying agent that forms a large number of gas-phase products during the reaction with nitrates, which makes it possible to regulate the microstructure and porosity of materials [26,27].

XRD results of the powder collected from the filter indicate the formation of a single-phase product (Figure 1). The diffraction peaks were matched with the $CaMnO_3$ phase according to the PDF#76-1132 database. $CaMnO_3$ has an orthorhombic crystal lattice with the space group $Pnma$ (62). No impurity phases were detected within the sensitivity of the method.

The calculated lattice parameters and unit cell volume are as follows: $a = 5.27481$, $b = 7.44839$, $c = 5.31953\,Å$, $V = 208.998\,Å^3$, which are consistent with the literature data [12,28–30]. The peak positions of the diffraction reflexes remained unchanged after sintering of the sample, while their intensities doubled. The formation of secondary phases was not found. It is worth noting that some studies report the formation of the marokite phase ($CaMn_2O_4$) after sintering, which is attributable to both the deviation of the composition from stoichiometry and the low temperature of synthesis and annealing [9,31]. Indeed, the compound of $CaMnO_3$ is one of the three-component stoichiometric phases according to the equilibrium diagram of the state of CaO-MnO, however, it differs in a narrow homogeneity interval [32]. A slight deviation in the ratio of Ca/Mn concentrations can contribute to the formation of marokite, which worsens the TE properties of the whole material. It is possible to avoid this effect and stabilize the $CaMnO_3$ phase by prolonged annealing at high temperatures [9]. In the case of SSCS, the reagents in the initial solution are mixed at the molecular level in a precisely specified ratio and are bound through the use of an organic component into a stable complex. The solid-phase product formation reaction occurs at high temperatures reaching $\sim 1700\,K$, and lasts about hundreds of ms [19], which creates favorable conditions for the formation of a single-phase $CaMnO_3$.

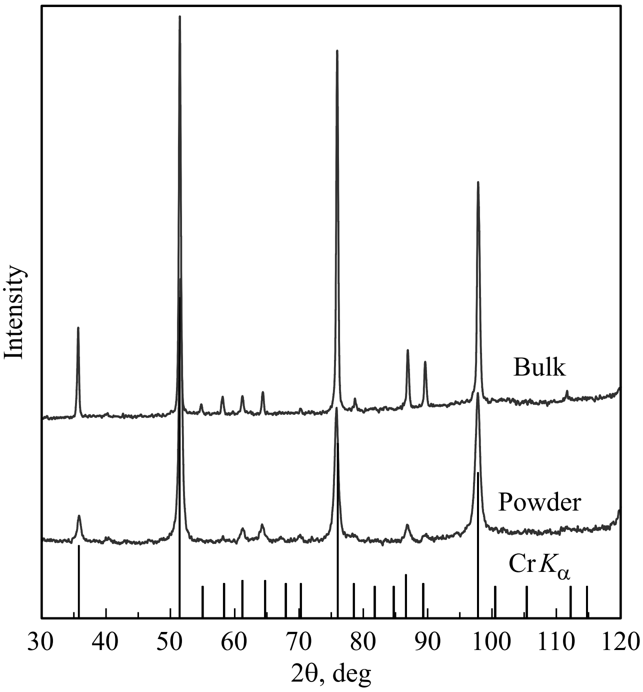

Figure 1. Diffraction patterns of the obtained $CaMnO_3$ specimens: powder (powder) and sintered sample.

Typical images of the microstructure of the samples are shown in Figure 2. The micrograph of the $CaMnO_3$ powder after synthesis indicates its spherical morphology (Figure 2, a). The size of the spheres varies from 100 nm to 4 μm. The surface consists of nanocrystallites, which form a porous framework. Some spheres appear to be destroyed with a cavity inside due to the abundant gas release. The wall thickness of the broken spheres varies from 50 to 100 nm. A large number of small pores are visible on the micrograph of the sintered sample, while the relative density of the material is 94%. Surface analysis of the fracture using the EDS method did not reveal any areas with a Ca/Mn ratio deviating from stoichiometric. The average composition of the sample is $Ca_{0.96}Mn_{0.95}O_{2.89}$.

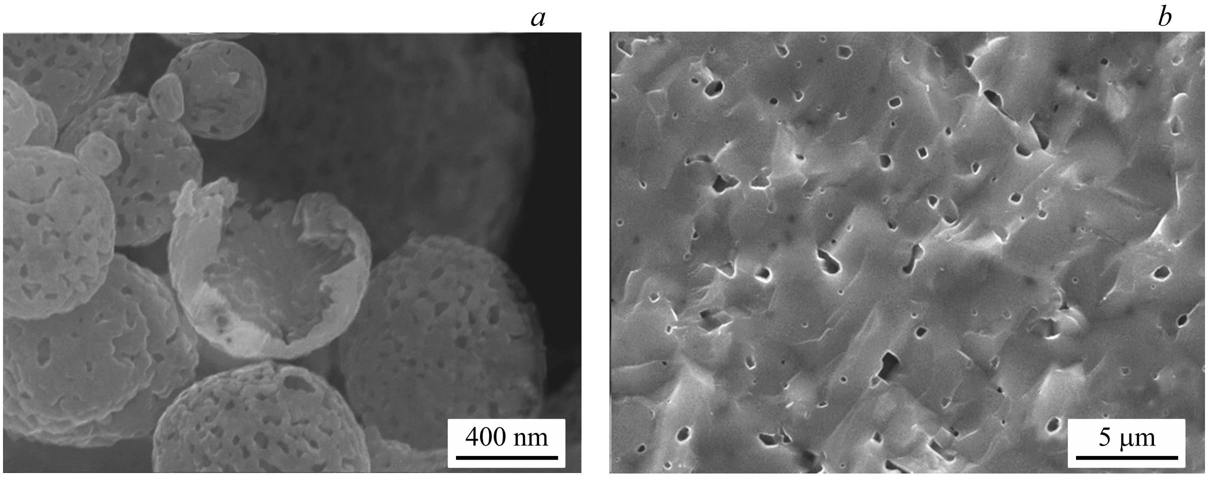

Figure 2. Micrographs obtained using a scanning electron microscope: *a* — powder after synthesis by the combustion of reaction aerosols, *b* — cleavage of the sintered sample.

3.2. Thermoelectric properties

The dependence of the total thermal conductivity (κ) of the sintered sample on temperature is shown in Figure 3, *a*. The sample demonstrates a smooth decrease of κ from $3.9\,\mathrm{W\cdot m^{-1}\cdot K^{-1}}$ at 300 K to $2.4\,\mathrm{W\cdot m^{-1}\cdot K^{-1}}$ at 1000 K, since the free path of phonons is inversely proportional to the absolute temperature. The thermal conductivity of the $CaMnO_3$ sample obtained by SSCS turns out to be comparable or lower than in the undoped samples of $CaMnO_3$ synthesized by other methods [15,17,28,33–35]. This result is attributable to the presence of many small pores in the SSCS sample of combustion of reaction aerosols, which enhances the processes of phonon scattering. However, when comparing the obtained results with the thermal conductivity values of $CaMnO_3$ samples doped with various metals, the κ of the SSCS samples is found to be higher. The most significant difference in κ is observed near room temperature, where the contribution of phonon scattering at grain boundaries is noticeably greater compared to phonon-phonon scattering, which plays a major role at high temperatures. The addition of doping elements in solid substitution solutions results in local distortions of the crystal lattice, which further reduces the contribution of the phonon subsystem to the overall thermal conductivity. It is also known that the oscillation amplitude of heavier ions is less than that of Ca^{2+}, and therefore phonons of various frequencies are scattered, thereby effectively reducing the phonon component of thermal conductivity. A decrease of phonon thermal conductivity directly results in a decrease of the total thermal conductivity in doped compositions [36].

The following equation was used to determine the lattice component of thermal conductivity (k_{lat})

$$\kappa_{\mathrm{lat}} = \kappa_{\mathrm{tot}} - \kappa_e, \quad (5)$$

where κ_e — the electronic component of thermal conductivity, which is determined by the Wiedemann–Franz law:

$$\kappa_e = L\sigma T, \quad (6)$$

where L is the Lorentz number. Typically, most studies use the value of $L = 2.44\cdot 10^{-8}\,\mathrm{W\cdot Ohm\cdot K^{-2}}$, which is valid only for metals and degenerate semiconductors. L was assumed in our calculations to be equal to $1.77\cdot 10^{-8}\,\mathrm{W\cdot Ohm\cdot K^{-2}}$ at room temperature, which was obtained from the equation of $L = 1.5 + \exp(-|S|/116)$ [37] taking into account experimental data for the Seebeck coefficient S. However, it should be noted that the minimum and maximum values of the Lorentz number in the calculation slightly affect the lattice part of the thermal conductivity because of the small contribution of the electronic component to the total thermal conductivity, changing it only by 3.8% for the limiting cases of a non-degenerate state [17]. In our case, the contribution of κ_e to κ_{tot} is $\sim 0.14\%$ near room temperature and 1.79% at 1000 K, which will also slightly affect κ_{lat} in the case of substitution limiting cases of the Lorentz number.

The decrease of the lattice thermal conductivity with the increase of temperature is a consequence of an increase of the probability of collision of phonons involved in the phenomenon of heat transfer, leading to transfer processes. A graph of the dependence $\kappa_{\mathrm{lat}}(T) \propto T^{-x}$ was plotted on a double logarithmic scale for the analysis of the predominant phonon scattering mechanism (Figure 3, *b*). It can be seen from Figure 3, *b* that the experimental results are better described by the dependence with $x = 0.5$, which corresponds to the scattering mechanism on point defects [38]. Such a mechanism in our study may be a consequence of oxygen vacancies, the presence of which is confirmed by a decrease of the volume of the crystal lattice [39].

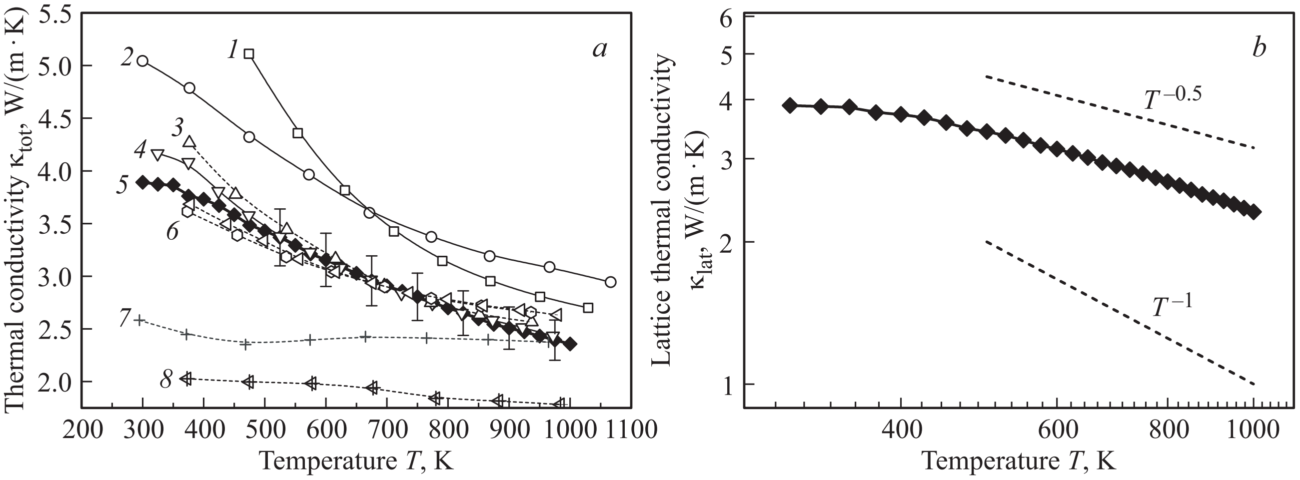

Figure 3. The temperature dependence of the total (a) and lattice (b) thermal conductivity of $CaMnO_3$ obtained by SSCS method (shaded diamonds). a provides literature data for: *1* — $CaMnO_3$ [17], *2* — $CaMnO_3$ [34], *3* — $CaMn_{0.99}W_{0.01}O_3$ [17], *4* — $CaMnO_3$ [11], *5* — $Ca_{0.96}Gd_{0.04}O_3$ [28], *6* — $Ca_{0.97}Yb_{0.015}Gd_{0.015}O_3$ [17], *7* — $Ca_{0.9}Nd_{0.1}MnO_3$ [35], *8* — $Ca_{0.95}Yb_{0.05}Mn_{0.98}Nb_{0.02}O_3$ [15]. The dotted lines on b show the dependences of $\kappa_{\text{lat}}(T)$ in the case of dominant phonon scattering at grain boundaries ($\kappa_{\text{lat}}(T) \sim T^{-1}$) and on point defects ($\kappa_{\text{lat}}(T) \sim T^{-0.5}$).

It is shown in Ref. [40] that the dependence corresponds to $\kappa_{\text{lat}} \sim T^{-1}$ in $CaMnO_3$, which the authors associate with phonon-phonon scattering. A slight deviation from $\kappa_{\text{lat}} \sim T^{-1}$ was recorded in the nominal composition of $Ca_{0.9}Y_{0.1}MnO_3$ and in the presence of oxygen vacancies in the undoped $CaMnO_3$, which is attributable to the impact of scattering of point defects due to the substitution of calcium cation in this system.

The temperature dependence of the electrical conductivity of $CaMnO_3$ obtained by SSCS is shown in Figure 4, a. The samp le exhibits semiconductor behavior ($d\sigma/dT > 0$), where σ increases from $10.4\,\text{S} \cdot \text{cm}^{-1}$ at room temperature to $26.4\,\text{S} \cdot \text{cm}^{-1}$ at 1000 K. The general appearance of the curve and the measured values of electrical conductivity are in good agreement with the results obtained in other studies of undoped $CaMnO_3$ [13,41]. At the same time, the electrical conductivity of doped samples is expected to be higher and decreases with the increase of the temperature, which is typical for degenerate semiconductors.

As shown above, the materials based on $CaMnO_3$ realize the mechanism of electrical conductivity of small polarons between ions of Mn^{3+} and Mn^{4+} [8,20], which is described by the Mott-Davis equation [9]:

$$\sigma = \frac{A}{T} \exp\left(-\frac{E_a}{k_B T}\right), \qquad (7)$$

where A — pre-exponential factor determined by the properties of the material, T — absolute temperature, E_a — activation energy of the hopping conduction mechanism, k_B — Boltzmann constant. Figure 4, b shows that the graph plotted in coordinates $\ln(\sigma T)$ from $1000/T$ straightens to the temperature of $T = 750\,\text{K}$, which is typical for materials with conductivity attributable to the small polaron hopping [36].

In our case, the occurrence of Mn^{3+} ions is associated with the presence of oxygen vacancies in the sample, while the undoped stoichiometric $CaMnO_3$ contains Mn^{4+} ions [21]. Doping with trivalent rare earth ions at the Ca position and (or) the occurrence of nonstoichiometry in oxygen results in an increase of the concentration of charge carriers. The presence of a noticeable number of ions Mn^{3+} introduces a large number of charge carriers and facilitates the movement of these charge carriers through the hopping mechanism [42]. Thus, electron hopes between Mn^{3+} and Mn^{4+} cause high values of electrical conductivity in doped and nonstoichiometric samples.

Charge carriers in hopping conductivity are thermally activated with an activation energy of E_a. For instance, $E_a = 0.167$ [43], 0.089 [20], 0.122 [21], 0.13–0.22 [9], 0.09 [11], 0.117 eV [44] is reported in the literature for an undoped composition. In our case, the activation energy of the polaron jump $E_a = 0.05\,\text{eV}$ was calculated at temperatures up to 750 K, which is significantly lower than the values given in the literature for undoped samples of $CaMnO_3$. However, the value $E_a = 0.05\,\text{eV}$ that we obtained is close to the activation energy for doped samples [23,45], which indicates a decrease of the energy barrier for polaron hopping, hence an increase of the concentration of charge carriers.

The values of electrophysical parameters in the literature differ because of different synthesis methods and sintering conditions of ceramics, which strongly affect the number of defects, such as grain boundaries, an increased number of pores, which also affects the mobility of charge carriers that are localized at the sites of defects.

$CaMnO_3$ has negative values of the Seebeck coefficient as a n-type semiconductor (Figure 4, c). The absolute values of the Seebeck coefficient of the obtained sample gradually

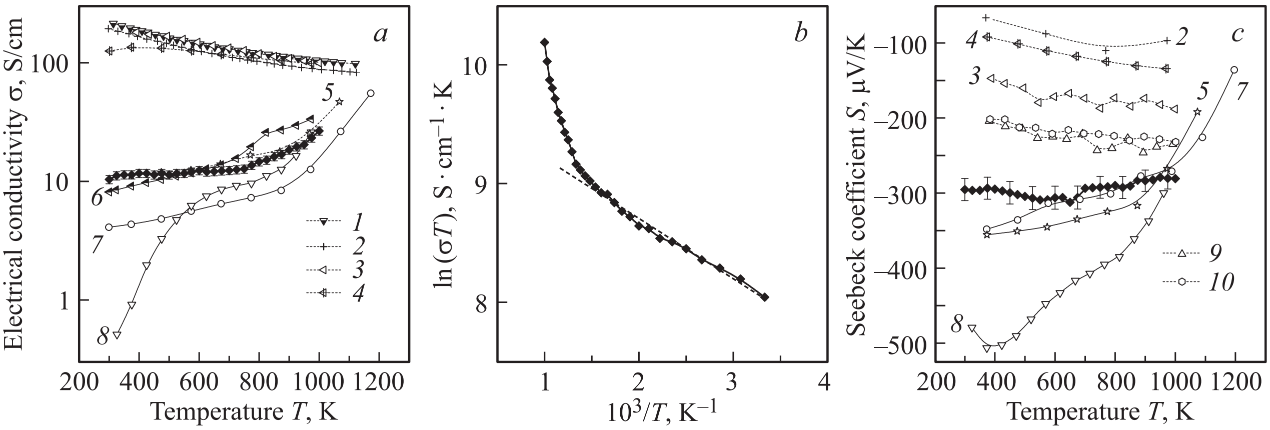

Figure 4. The temperature dependence (*a*) electrical conductivity CaMnO$_3$, (*b*) dependence $\ln(\sigma T)$ on $1000/T$ (dotted line shows the dependence characteristic of the electrical conductivity carried out due to jumps of small polarons), (*c*) Seebeck coefficient (the shaded diamonds correspond to the values obtained in this work) in comparison with the literature data: *1* — Ca$_{0.9}$Tb$_{0.1}$MnO$_3$ [35], *2* — Ca$_{0.9}$Nd$_{0.1}$MnO$_3$ [35], *3* — Ca$_{0.96}$Gd$_{0.04}$O$_3$ [28], *4* — Ca$_{0.95}$Yb$_{0.05}$Mn$_{0.98}$Nb$_{0.02}$O$_3$ [15], *5* — CaMnO$_3$.

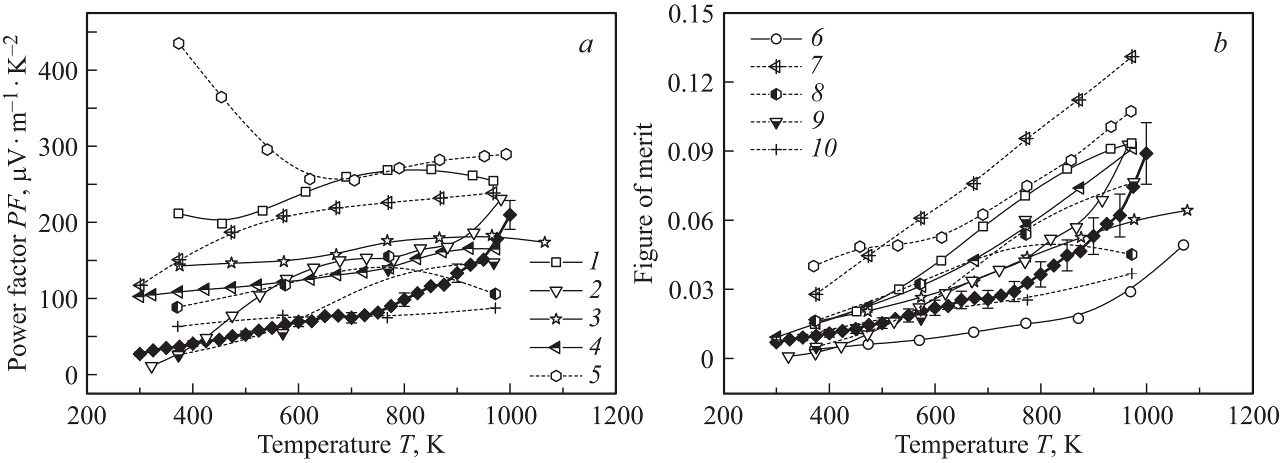

Figure 5. Temperature dependence (*a*) power factor, (*b*) thermoelectric Q-factor of CaMnO$_3$ obtained by the combustion of reaction aerosols (the shaded diamonds correspond to the values obtained in this work) in comparison with the literature data: *1* — CaMnO$_3$ [17], *2* — CaMnO$_3$ [11], *3* — CaMnO$_3$ [13], *4* — CaMnO$_3$ [41], *5* — Ca$_{0.98}$Yb$_{0.01}$Gd$_{0.01}$O$_3$ [17], *6* — CaMnO$_3$ [34], *7* — Ca$_{0.95}$Yb$_{0.05}$Mn$_{0.98}$Nb$_{0.02}$O$_3$ [15], *8* — Ca$_{0.9}$Ho$_{0.1}$MnO$_3$ [35], *9* — Ca$_{0.9}$Tb$_{0.1}$MnO$_3$ [35], *10* — Ca$_{0.9}$Nd$_{0.1}$MnO$_3$ [35].

decrease with temperature from $S \sim 295\,\mu\mathrm{V}\cdot\mathrm{K}^{-1}$ at room temperature to $\sim 280\,\mu\mathrm{V}\cdot\mathrm{K}^{-1}$ at 1000 K. A similar trend was reported in Ref. [46,47].

The value of Seebeck coefficient decreases with an increase of doping additives since it has an inverse dependence on the concentration of charge carriers. Accordingly, the samples in Ref. [15,17,35] demonstrate reduced values of S over the entire range of measured temperatures relative to the sample of CaMnO$_3$ synthesized by SSCS.

The maximum power factor $PF = S^2\sigma$ (Figure 5, *a*) for the presented sample is $161\,\mu\mathrm{V}\cdot\mathrm{m}^{-1}\cdot\mathrm{K}^{-2}$, which is comparable or even higher than the values for undoped samples [13,41] and some doped samples [35], which can be explained by higher values of the absolute Seebeck coefficient in the synthesized material. However, the values of PF of this sample are inferior, for example, to compositions with Yb^{3+} [15,17] because of relatively low electrical conductivity, since the electron concentration introduced by doping plays a decisive role in the electrical conductivity of these materials.

The maximum value $zT = 0.09$, shown in Figure 5, *b*, was reached at 1000 K, which is close to the literature data [13,17,28,33,34,41], and also demonstrates the average values relative to doped samples. However, the resulting composition has advantages among the other considered compositions because of a significant reduction of the ceramics production time, as well as low cost, without doping additives with expensive elements.

4. Conclusion

A single-phase spherical powder of CaMnO$_3$ was obtained by spray solution combustion synthesis using glycine, which performs important functions in the formation of a crystalline solid-phase product. The powder was consolidated by cold pressing followed by sintering in air without applying a load for obtaining a bulk material. The bulk $CaMnO_3$ sample showed lower values of thermal conductivity relative to previously published papers due to the special microstructure and effective scattering on oxygen vacancies.

The electrical conductivity does not significantly increase despite the decrease of the activation energy of the polaron hopping, however, the absolute values of the Seebeck coefficient remain quite high over the entire measured temperature range, while S sharply decreases in doped samples, as a rule, because of a shift of the equilibrium of Mn^{3+}/Mn^{4+} towards Mn^{3+}, which results in the generation of charge carriers and a decrease of their mobility.

The proposed method is potentially scalable and allows obtaining oxide thermoelectric materials with the efficiency comparable to the efficiency of these compounds obtained by much more labor-intensive methods.

Funding

This study was financially supported by the Russian Science Foundation (project No. 22-79-10278).

Conflict of interest

The authors declare that they have no conflict of interest.

References

[1] B. Srinivasan, A. Gellé, F. Gucci, C. Boussard-Pledel, B. Fontaine, R. Gautier, H. J.-F. Halet, M.J. Reece, B. Bureau. Inorg. Chem. Front., **6** (1), 63 (2019).

[2] G. Rogl, P. Rogl. Curr. Opin. Green Sustain. Chem., **4**, 50 (2017).

[3] Yu.I. Ravich, B.A. Efimova, I.A. Smirnov. *Metody issledovaniya poluprovodnikov v primenenii k hal'kogenidam svintsa PbTe, PbSe i PbS* (M., Nauka, 1968). (in Russian).

[4] N.V. Nong, C.-J. Liu, M. Ohtaki. J. Alloys Compd., **509** (3), 977 (2011).

[5] H. Colder, E. Guilmeau, C. Harnois, S. Marinel, R. Retoux, E. Savary. J. Eur. Ceram. Soc., **31** (15), 2957 (2011).

[6] H. Muta, K. Kurosaki, S. Yamanaka. J. Alloys Compd., **350** (1−2), 292 (2003).

[7] M. Acharya, S.S. Jana, M. Ranjan, T. Maiti. Nano Energy, **84**, 105905 (2021).

[8] L. Bocher, M.H. Aguirre, D. Logvinovich, A. Shkabko, R. Robert, M. Trottmann, A. Weidenkaff. Inorg. Chem., **47** (18), 8077 (2008).

[9] S.O.A. De Torres, D. Thomazini, G.P. Balthazar, M.V. Gelfuso. Mater. Res., **23** (5), e20200169 (2021).

[10] A. Baranovskiy, Y. Amouyal. J. Alloys Compd., **687**, 562 (2016).

[11] K.K. Li, Z.Y. Liu, F.P. Zhang, J.X. Zhang, X.Y. Yang, J.W. Zhang, J.L. Shi, G. Ren, T.W. He, J.J. Duan. J. Alloys Compd., **808**, 151476 (2019).

[12] P. Thiel, J. Eilertsen, S. Populoh, G. Saucke, M. Döbeli, A. Shkabko, L. Sagarna, L. Karvonen, A. Weidenkaff. J. Appl. Phys., **114** (24), 243707 (2013).

[13] Y.-H. Zhu, W.-B. Su, J. Liu, Y.-C. Zhou, J. Li, X. Zhang, Y. Du, C.-L. Wang. Ceram. Int., **41** (1), 1535 (2015).

[14] M. Mouyane, B. Itaalit, J.Ô. Bernard, D. Houivet, J.G. Noudem. Powder Technol., **264**, 71 (2014).

[15] R. Kabir, T. Zhang, R. Donelson, D. Wang, R. Tian, T.T. Tan, B. Gong, S. Li. Phys. Status Solidi A, **211** (5), 1200 (2014).

[16] G. Xu. Solid State Ion., **171** (1−2), 147 (2004).

[17] R. Löhnert, J. Töpfer. J. Solid State Chem., **315**, 123437 (2022).

[18] F. Azough, A. Gholinia, D.T. Alvarez-Ruiz, E. Duran, D.M. Kepaptsoglou, A.S. Eggeman, Q.M. Ramasse, R. Freer. ACS Appl. Mater. Interfaces, **11** (36), 32833 (2019).

[19] G.V. Trusov, A.B. Tarasov, E.A. Goodilin, A.S. Rogachev, S.I. Roslyakov, S. Rouvimov, K.B. Podbolotov, A.S. Mukasyan. J. Phys. Chem. C, **120** (13), 7165 (2016).

[20] M.E.M. Jorge, M.R. Nunes, R.S. Maria, D. Sousa. Chem. Mater., **17** (8), 2069 (2005).

[21] A. Vijay, R. Suhashini, R. Jose, S.C. Prasanth, K.V. Saravanan. AIP Conf. Proc., **2220** (1), 080029 (2020).

[22] M. Schrade, R. Kabir, S. Li, T. Norby, T.G. Finstad. J. Appl. Phys., **115** (10), 103705 (2014).

[23] A. Vijay, C. P. S, R. Jose, V. Saravanan. RSC Advaces, **13** (28), 19651 (2023).

[24] G.V. Trusov, A.B. Tarasov, D.O. Moskovskikh, A.S. Rogachev, A.S. Mukasyan. J. Alloys Compd., **779**, 557 (2019).

[25] F.P. Zhang, X. Zhang, Q.M. Lu, J.X. Zhang, Y.Q. Liu. J. Alloys Compd., **509** (10), 4171 (2011).

[26] A. Varma, A.S. Mukasyan, A.S. Rogachev, K.V. Manukyan. Chem. Rev., **116** (23), 14493 (2016).

[27] A.S. Mukasyan, D.O. Moskovskikh, A.A. Nepapushev, J.M. Pauls, S.I. Roslyakov. J. Eur. Ceram. Soc., **40** (7), 2512 (2020).

[28] R. Löhnert, M. Stelter, J. Töpfer. Mater. Sci. Eng. B, **223**, 185 (2017).

[29] S. Paengson, P. Pilasuta, K. Singsoog, W. Namhongsa, W. Impho, T. Seetawan. Materials Today Proceedings, **4** (5), 6289 (2017).

[30] P.N. Santhosh, J. Goldberger, P.M. Woodward, T. Vogt, W.P. Lee, A.J. Epstein. Phys. Rev. B, **62** (22), 14928 (2000).

[31] R. Kabir, T. Zhang, D. Wang, R. Donelson, R. Tian, T.T. Tan, S. Li. J. Mater. Sci., **49** (21), 7522 (2014).

[32] H.S. Horowitz, J.M.L. Horowitz. Mater. Res. Bulletin, **13** (12), 1359 (1978).

[33] T. Liu, J. Chen, M. Li, G. Han, C. Liu, D. Zhou, J. Zou, Z.-G. Chen, L. Yang. Chem. Eng. J., **408**, 127364 (2021).

[34] S.P. Singh, N. Kanas, T.D. Desissa, M.A. Einarsrud, T. Norby, K. Wiik. J. Eur. Ceram. Soc., **40** (4), 1344 (2020).

[35] R. Funahashi, A. Kosuga, N. Miyasou, E. Takeuchi, S. Urata, K. Lee, H. Ohta, K. Koumoto, 26th Int. Conf. on Thermoelectrics (Jeju Island, 3−5 June, South Korea) [IEEE, **1**, 124 (2007)].

[36] T. Yang, T. Cheng. RSC Advaces, **7** (71), 44659 (2017).

[37] A. Novitskii, G. Guélou, A. Voronin, T. Mori, V. Khovaylo. Scr. Mater., **187**, 317 (2020).

[38] M. Schrade, K. Berland, S.N.H. Eliassen, M.N. Guzik, C. Echevarria-Bonet, M.H. Sørby, P. Jenuš, B.C. Hauback, R. Tofan, A.E. Gunnæs, C. Persson, O.M. Løvvik, T.G. Finstad. Sci. Rep., **7** (1), 13760 (2017).

[39] C.S. Huang, H. Fang, Z.H. Xu, X. Zheng, X.X. Ruan. Results Phys., **13**, 102337 (2019).

[40] G.-K. Ren, J.-L. Lan, K.J. Ventura, X. Tan, Y.-H. Lin, C.-W. Nan. Npj Comput. Mater., **2** (1), 16023 (2016).

[41] R. Kabir, R. Tian, T. Zhang, R. Donelson, T.T. Tan, S. Li. J. Alloys Compd., **628**, 347 (2015).

[42] Y. Wang, Y. Sui, X. Wang, W. Su. J. Phys. D: Appl. Phys., **42** (5), 055010 (2009).

[43] A. Vijay, R. Jose, C. Prasanth S, V. P, K. Venkata Saravanan. Materials Today Proceedings, **64**, 431 (2022).

[44] L.T. Hung, N.V. Nong, L. Han, D.L. Minh, K.A. Borup, B.B. Iversen, N. Pryds, S. Linderoth. J. Mater. Sci., **48**, 2817 (2013).

[45] J. Lan, Y.-H. Lin, H. Fang, A. Mei, C.-W. Nan, Y. Liu, S. Xu, M. Peters. J. Am. Ceram. Soc., **93** (8), 2121 (2010).

[46] C. Li, Q. Chen, Y. Yan. Materials, **11** (10), 1807 (2018).

[47] S. BerbethMary, K. Nalini, K. Rajalakshmi. Materials Today Proceedings, **57**, 2344 (2022).

Translated by A.Akhtyamov